

CORALIE radial-velocity search for companions around evolved stars (CASCADES)

V. Three planetary companions and achievable precision

P. Figueira^{1,2*}, E. Fontanet², J. P. Faria², M. Esseldeurs³, E. Friden², A. Leleu², R. Luque¹,
G. Ottoni², D. Ségransan², M. Stalport^{4,5}, S. Tavella^{2,6}, S. Udry²

¹ Instituto de Astrofísica de Andalucía-CSIC, Glorieta de la Astronomía s/n, 18008 Granada, Spain

² Observatoire Astronomique de l'Université de Genève, Chemin Pegasi 51b, 1290 Versoix, Switzerland

³ Instituut voor Sterrenkunde, KU Leuven, Celestijnenlaan 200D, 3001 Leuven, Belgium

⁴ Space sciences, Technologies and Astrophysics Research (STAR) Institute, Université de Liège, Allée du 6 Août 19C, 4000 Liège, Belgium

⁵ Astrobiology Research Unit, Université de Liège, Allée du 6 Août 19C, 4000 Liège, Belgium

⁶ European Southern Observatory, Alonso de Córdova 3107, Vitacura, Región Metropolitana, Chile

Received 20 March 2026; dd June 2026

ABSTRACT

Aims. We expand the planetary census around massive stellar hosts through a long-term campaign of high-precision radial velocity (RV) measurements on evolved stars.

Methods. We analyse data acquired with the CORALIE spectrograph covering 15–18 years on HD 125136, HD 127195, and HD 220218. Stellar parameters are derived through different methods for a comprehensive characterization of each star. We then evaluate the presence of planetary signals in the RV time series using the Bayesian inference tool *kima*. Finally, we design an observing strategy aimed at mitigating the impact of pulsations on evolved stars and test its effectiveness on the low-luminosity red giant HD 127195.

Results. We detect signals that are accurately modelled by Keplerian curves in the RV data of the three stars: one on HD 125136, two on HD 127195, and one on HD 220218. While the signals on the first two stars seem to be of planetary origin, the signal on the third one shows several signs of stellar activity. We therefore identify a planetary companion around HD 125136 with a minimum mass of $2.26 M_{\text{Jup}}$ on an 850 d orbit, and on HD 127195 we identify a system composed of planets with $0.66 M_{\text{Jup}}$ and $0.78 M_{\text{Jup}}$ with orbital periods of 535 d and 834 d, respectively.

Conclusions. We detect three massive planets around two low-luminosity red giant stars in a region of the parameter space that is poorly populated in both stellar mass and planetary orbital periods. The dedicated observing campaign on HD 127195 showcases how stellar pulsations can be efficiently averaged out to below 5 m s^{-1} in low-luminosity giant stars.

Key words. planets and satellites: detection – methods: observational – techniques: radial velocities – stars: individual: HD 125136, HD 127195, HD 220218

1. Introduction

With approximately 6200 planets known¹, the search for exoplanets is now mainstream science. While the search for planets around low-mass stars has received considerable attention, the study of planets around stars more massive than our Sun has not. Currently, there are only ~ 1300 planets detected around stars with a mass greater than $1.1 M_{\odot}$, which corresponds to about 20% of the planets known.

The study of planets around stars more massive than our Sun is nonetheless of undisputed scientific relevance. Because stellar mass is a proxy for protoplanetary disk mass and lifetime, planets around massive stars provide key constraints on planet formation efficiency, migration, and atmospheric evolution. Planetary parameters are a function of stellar mass (e.g. Alibert et al. 2005, 2011; Kennedy & Kenyon 2008) and planetary demographics features such as the radius-gap (Fulton et al.

2017; Van Eylen et al. 2018) are also strongly dependent on the host mass, as demonstrated by Venturini et al. (2024).

Unfortunately, the higher effective temperature of massive stars when compared with solar-mass stars reduces the number of photospheric lines that can be used for precise radial velocity (RV) determination. Moreover, the median rotational velocity increases with mass (e.g. McNally 1965). A-type stars typically exhibit projected rotational velocities $v \sin i \gtrsim 100 \text{ km s}^{-1}$, while F-type stars show a wide distribution, often reaching several tens of km s^{-1} . The survey of planets around AF main-sequence stars with the HARPS spectrograph confirmed this dependence of achievable precision on stellar mass (Borgniet et al. 2019). The authors reported a median RV dispersion of 60 m s^{-1} for a sample with a median photon-noise uncertainty of 14 m s^{-1} , with both quantities strongly dependent on stellar mass, spectral type, and rotational velocity.

When targeting stars in the $1.1\text{--}5 M_{\odot}$ mass range, most campaigns focus on old stars that moved out of the main sequence (e.g. Lovis & Mayor 2007). These evolved stars are more lumi-

* Corresponding author: pedro.figueira@iaa.es

¹ Check exoplanet.eu for an updated value.

nous, have a larger radius and a lower effective temperature than their main sequence counterparts; they have historically been labelled as giants in opposition to the main-sequence dwarfs. The difference in observables comes from the star burning hydrogen in a shell around an inert helium core (and later, for sufficiently massive stars, igniting helium in the core), that pushes the stellar layers outwards and modifies the properties of the photosphere.

We have been pursuing a long-term RV follow-up of evolved stars, named CASCADES. The program and first results were presented by [Ottoni et al. \(2022\)](#), with three follow-up works on stellar and planetary characterization by [Buldgen et al. \(2022\)](#), [Pezzotti et al. \(2022\)](#) and the latest by [Fontanet et al. \(2025\)](#).

In this work we focus on targets on the early phase of the red giant evolutionary stage. These stars are often called low-luminosity red giants and exhibit a comparatively lower RV jitter than their higher-luminosity counterparts. We use this characteristic to our advantage to explore the planets population detectable in RV. These systems provide a crucial bridge between planet populations around solar-type stars and those forming in the higher-mass, shorter-lived disk environments of intermediate-mass stars.

We start with the stellar characterization and the properties of CORALIE data in Section 2. In Section 3 we study the signals present in our RVs and their nature. In Section 4 we present a dedicated campaign on one of our subgiants aimed at reducing the impact of pulsations on the error budget, and evaluate its efficiency. We discuss and contextualize our results in Section 5 and wrap up our conclusions in Section 6.

2. Target properties and data

In Fig. 1 we represent the CASCADES survey stars against the sample of bright ($G < 12$ mag) nearby ($d < 200$ pc) *Gaia* Data Release 3 ([Gaia Collaboration et al. 2016, 2023](#), henceforth DR3) stars. We use an observational Hertzsprung–Russell (HR) diagram and a Kiel diagram to represent the evolutionary stages graphically. To transform *Gaia*'s G into V we used Table 5.9 of *Gaia* DR3 documentation². For display purposes, we selected only objects with $2000 < T_{\text{eff}} < 10\,000$ K, and $-0.5 < B - V < 2.5$. While in the HR diagram the evolved stars depart from the main sequence becoming brighter and redder, in the Kiel diagram the giant branch is clearly separated toward lower $\log g$ and lower T_{eff} (e.g. [Fuhrmann 1998](#); [Takeda et al. 2005](#)).

2.1. Target properties

In the past, several exoplanet programs have used absolute magnitude and colour cuts to select for subgiant stars (e.g. [Johnson et al. 2007](#)). These stars have left the main sequence, exhibiting a lower temperature and higher luminosity, but have not yet ascended into the red giant branch, showing a particularly low RV jitter for an evolved star. We selected stars from the CASCADES catalogue by applying the constraints $1.8 < M_V < 2.5$ mag and $0.78 < B - V < 1.06$ mag, following the prescription of [Wittenmyer et al. \(2011\)](#). From the 26 stars satisfying these criteria, we identified three stars worth studying in detail: HD 125136, HD 127195, and HD 220218. These targets stood out for having a sufficient number of RV measurements for detailed analysis (≈ 40 epochs) and an RV scatter of several

tens of m s^{-1} , compatible with the signature induced by a Jupiter-mass companion.

For each star we compile the parameters published in [Ottoni et al. \(2022\)](#), and complement these with both the *Gaia* DR3 parameters and parameters derived with ARIADNE ([Vines & Jenkins 2022](#)). ARIADNE is a Python package for fitting spectral energy distributions using Bayesian inference to derive fundamental stellar parameters from multi-band photometry. The data collection, parameter derivation, and resulting stellar parameters for each case are presented in Appendix A. A comparison of the results, presented in Table A.2 and illustrated by Fig. A.1 reveals both similarities and differences. Except for a few cases, the stellar parameters derived for a given star agree across methods within the quoted uncertainties. In the remainder of the paper we adopt the CASCADES values, which are available for all stars and parameters.

Subgiant stars typically have $R \sim 1.2\text{--}3.5 R_{\odot}$ and $\log g \sim 3.7\text{--}4.1$ (e.g. [Bryant & Van Eylen 2025](#)). The radii that we measured for our targets is larger and the surface gravity lower than those of subgiant stars. Moreover, our targets are not located on the horizontal subgiant branch in the HR diagram, but above it. We classify then these stars as low-luminosity giant stars.

To the best of our knowledge, there is no prior literature providing a detailed characterization of these stars, nor dedicated studies of planet occurrence around them.

2.2. CORALIE spectrograph and data properties

The CORALIE spectrograph is a twin of the ELODIE spectrograph ([Baranne et al. 1996](#)), used to detect 51 Peg b ([Mayor & Queloz 1995](#)). Mounted on the 1.2 m Swiss Euler telescope at La Silla, it has been in continuous operation since 1998 ([Queloz et al. 2000](#)) and contributed to more than 200 refereed works³.

CORALIE is an optical (381 to 681 nm) fibre-fed high-resolution ($R \sim 60\,000$) echelle spectrograph. In parallel with the science fibre (A), a second calibration one (B) is used to collect either skylight for background measurement, or light from a RV reference: either a Th–Ar lamp of a back-illuminated Fabry–Pérot (FP) etalon. This reference is used to measure the instrumental drift, a first-order estimation of the wavelength solution shift due to environmental changes. Since the light collected by the two fibres follows parallel and very similar optical paths, one can assume that the shift measured in B is likewise present in the stellar spectra collected through A. The instrument's drift is then corrected by subtracting from the science target RV the contemporaneous drift.

The data acquired with CORALIE are reduced with an automatic data reduction software (DRS), which ensures a homogeneous RV derivation. RVs are calculated via the cross-correlation function method, as described in [Baranne et al. \(1996\)](#) and expanded upon to include weighted masks ([Pepe et al. 2002](#)). Since our three stars have $T_{\text{eff}} \approx 5000$ K, corresponding to early-K spectral types, we used the K5 template mask as the closest available option. Upon reduction, the data are injected into the DACE database and available through the dedicated interface⁴.

The cross-correlation function is provided with the quantities full-width at half-maximum (FWHM), line contrast, and bisector inverse slope (BIS, see [Queloz et al. 2001](#)), that tracks shape variations of the photospheric lines. In addition, DACE per-

² https://gea.esac.esa.int/archive/documentation/GDR3/Data_processing/chap_cu5pho/cu5pho_sec_photSystem/cu5pho_ssec_photRelations.html

³ Data recovered with the [The SAO Astrophysics Data System](#) on June 2026.

⁴ <https://dace.unige.ch/radialVelocities/>

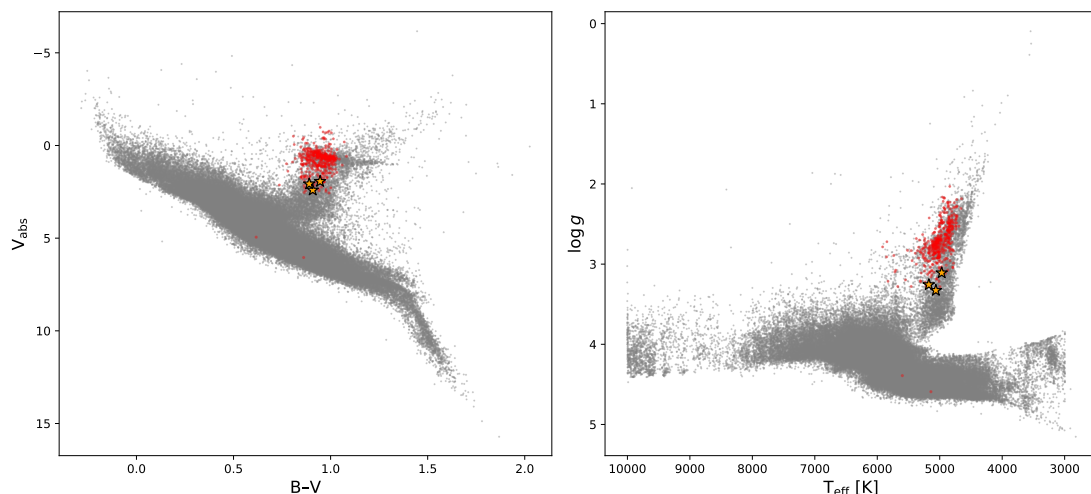


Fig. 1: Hertzsprung–Russell (*left*) and Kiel (*right*) diagrams for the CASCADES stars (red dots) and the three stars analysed in this work (orange stars), against the *Gaia* DR3 sample (gray dots).

forms a post-processing calculation of H_α activity index. The index is calculated over a narrow wavelength region, following the prescription and wavelength limits defined in Cincunegui et al. (2007) and Boisse et al. (2009). The customary Na I and Ca II activity indices were not used; the low chromospheric flux when compared to the strong contamination from the FP spectra make the measurements useless.

CORALIE underwent several interventions that changed its optical properties or wavelength dispersion characteristics. As such the time series are divided into independent datasets, treated as different instruments:

- COR98, DRS-3.3: the original CORALIE setup (see Baranne et al. 1996; Queloz et al. 2000).
- COR07, DRS-3.4: in April–May 2007 the fibre link and cross-disperser optics were replaced, leading to an increase in resolution and throughput. Since the double-scrambler was removed, the illumination stability properties were reduced and its contribution to the RV budget increased, leading to a slightly lower RV precision than for COR98. For further information see Ségransan et al. (2010).
- COR14, DRS-3.8: in November 2014 octagonal fibers were installed for improved light scrambling (without reducing throughput) and an FP was installed for simultaneous drift measurement in fibre B, replacing the Th–Ar lamp that had been used for this role, (along with being used for wavelength solution, as is customary).
- COR24, DRS-3.8: On 15 October 2024 an RV offset was introduced due to a change of the Th–Ar lamp.

The instrument has shown a long-term RV precision of around 5 m s^{-1} (Ségransan et al. 2010).

3. Planetary signals in RVs

The CORALIE RVs and associated quantities were retrieved from the DACE database using the `arvi` package⁵. In our analysis, we discarded observations with photon noise larger than 30 m s^{-1} (associated with very poor weather conditions) or for which the instrument drift was not properly corrected. The latter is identified using the drift quality control (QC) flag, and a complete explanation is presented in Appendix B.

⁵ <https://github.com/j-faria/arvi>

Table 1: Simple statistics for the different RV datasets acquired.

Star	Dataset	Δt [d]	N_{points}		avg. err [m s^{-1}]	w. rms
			QC _{pass}	QC _{fail}		
HD 125136	full set	5552.9	45	4	5.4	27.4
	COR98	27.0	3	0	4.0	6.5
	COR07	2541.0	21	1	4.9	26.6
	COR14	2527.0	21	3	6.0	31.1
HD 127195	full set	6737.6	81	5	5.2	15.6
	COR98	31.0	3	0	3.5	7.4
	COR07	2576.9	24	1	5.0	15.5
	COR14	3316.9	46	3	5.3	16.5
HD 220218	full set	172.6	8	1	5.8	13.1
	COR07	5141.0	54	4	7.7	28.2
	COR14	1206.7	11	0	6.9	43.9
	COR24	3295.0	31	4	7.7	21.8
	COR24	290.2	12	0	8.7	16.7

3.1. Simple statistics and general properties

The stars were observed for a total timespan of 15–18 years, and each star’s time series, shown in Fig. 2, contains between 45 and 81 points. For each star and dataset we provide simple summary statistics in Table 1. The average (photon-noise) RV uncertainty of each star’s full dataset is $5\text{--}8 \text{ m s}^{-1}$, comparable to or larger than the expected instrumental stability. Yet, the scatter, measured through the weighted root-mean-square (rms) is $16\text{--}28 \text{ m s}^{-1}$, in excess of both formal uncertainties and the instrument stability level. The difference between these quantities points towards an additional signal or unaccounted source of noise.

3.2. Periodic signals and correlation with activity indicators

We computed the generalized Lomb-Scargle periodogram (GLS) as introduced by Zechmeister & Kürster (2009) and implemented in `astropy`. To evaluate the significance of each signal we used the false-alarm probability (FAP) as defined by Baluev (2008). We chose two FAP threshold probabilities of 1% and

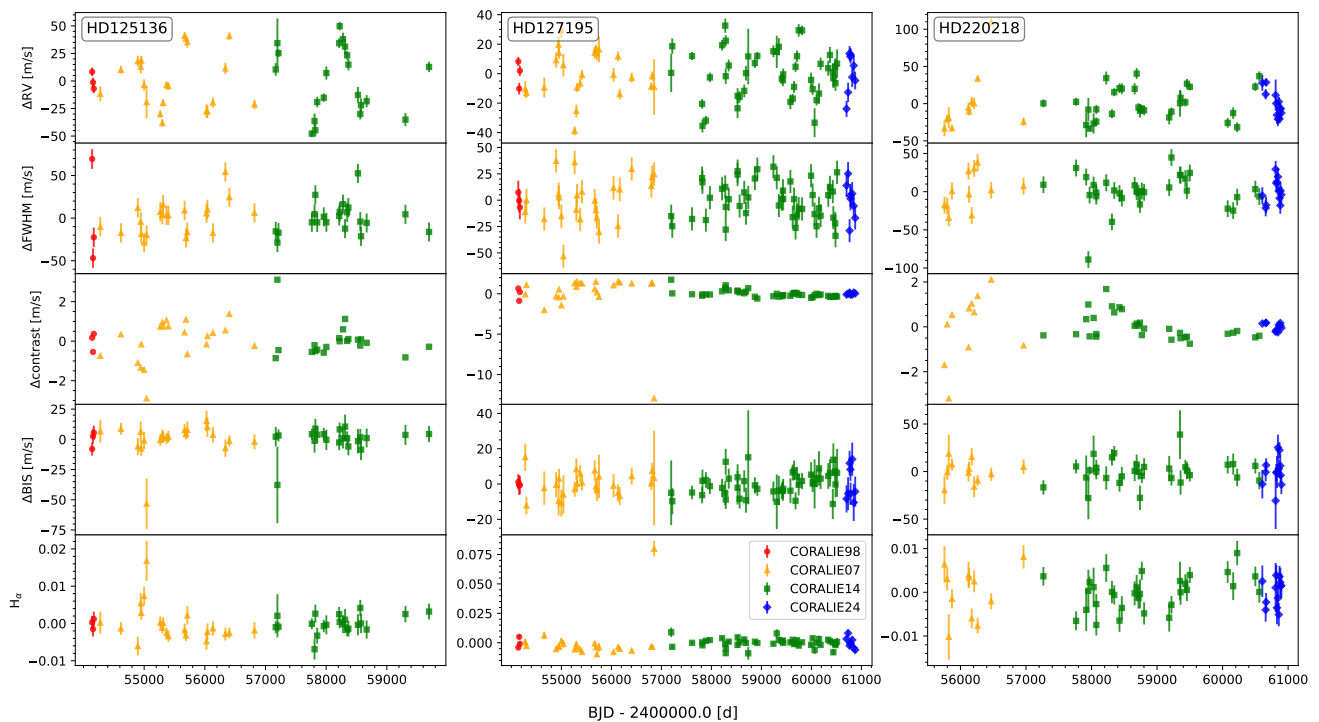


Fig. 2: Timeseries of RV and activity indicators: FWHM, contrast, BIS, and $H\alpha$ (top to bottom) for the stars HD 125136 (left), HD 127195 (center), and HD 220218 (right). The different CORALIE datasets are represented as different colours and symbols.

0.1% and a maximum frequency of 1 d^{-1} for the GLS and FAP calculations. The GLS periodogram for the different RV sets is shown in Fig. 3, along with the FAP thresholds. The window function, estimated by setting the measured signal at 1.0 (see VanderPlas 2018), is shown in the bottom row.

Each star shows a significant periodicity at the 0.1% FAP level: 848 d, 533 d, and 1039 d. In parallel, the window function shows a clear periodicity at around one year, caused by the annual visibility window of the targets from La Silla.

In addition to the most significant peak, the periodogram of HD 125136 shows several alias periods caused by the annual sampling window. Using the formalism described by VanderPlas (2018), 256 d and 647 d are the typical aliases, identified with $(n = 1, m = 1)$. The peak and bump at 1228 d and 2735 d correspond to $(n = 1, m = 3)$ and $(m = 2, n = -1)$, respectively. The integer m being larger than one comes from a high-order harmonic of the true frequency, and the negative n comes from the peak alias crossing into the negative frequency regime and being reflected into the positive frequency range, as discussed by VanderPlas (2018). This representation of the peak series as several aliases only demonstrates the presence of an underlying signal; from the frequency analysis it is not possible to separate original and aliased periods.

HD 127195 shows a second peak at 832 d, reaching the 0.1% significance threshold. We could not identify any plausible alias near to this period and interpret this signal as real.

The activity indicators FWHM, contrast, BIS and $H\alpha$ do not show significant periodic signals. However, for HD 127195 the FWHM has a marginal peak near the 1% FAP level, for a period of approximately one year.

A correlation between RVs and an activity indicator usually points towards an activity-induced RV signal (e.g., Figueira et al. 2013). We check for correlations between the RVs and the FWHM, bisector, contrast and $H\alpha$ indicators using the Pearson

Correlation coefficient. The coefficient values are shown in the radar chart in Fig 4, for a one-shot representation of correlations for a given star. The different indicators exhibit weak to no correlations with RV for the three stars.

The correlation coefficient for FWHM, BIS and $H\alpha$ remain below 0.2 for the three stars. For the contrast, for the stars HD 125136, HD 127195 and HD 220218 the values are approximately 0.3, 0.1, and 0.45, respectively. The two first values represent weak correlations, with the contrast-RV correlation for HD 220218 being in the range of moderate correlation. However, a direct interpretation of the value significance remains difficult.

Studying the presence of periodic signals in the RVs using GLS is insightful but not fully conclusive. The Keplerian orbits only become sinusoidal when the eccentricity is zero. The working hypothesis on the noise level, until now assumed as purely photon noise, also shift the FAP threshold levels considerably. Moreover, the absence of correlation between activity indicators and RV is not proof that the signals is not of stellar nature. A full analysis requires the evaluation of a model containing Keplerian signals and noise components.

3.3. kima analysis

We used the package *kima*⁶ (Faria et al. 2018) to model the planetary orbital parameters, stellar systemic velocity, and instrument-specific noise and RV offset values. *kima* uses the diffusive nested sampling algorithm from Brewer et al. (2009) to sample from the parameter posterior distribution; this delivers an estimate for the marginal likelihood for each model and allows direct Bayesian model comparison via the marginal likelihoods (see e.g., Brewer 2014; Feroz et al. 2011). In this context, the number of planets N_p is a parameter that can be left free or

⁶ <https://github.com/j-faria/kima-org/kima>

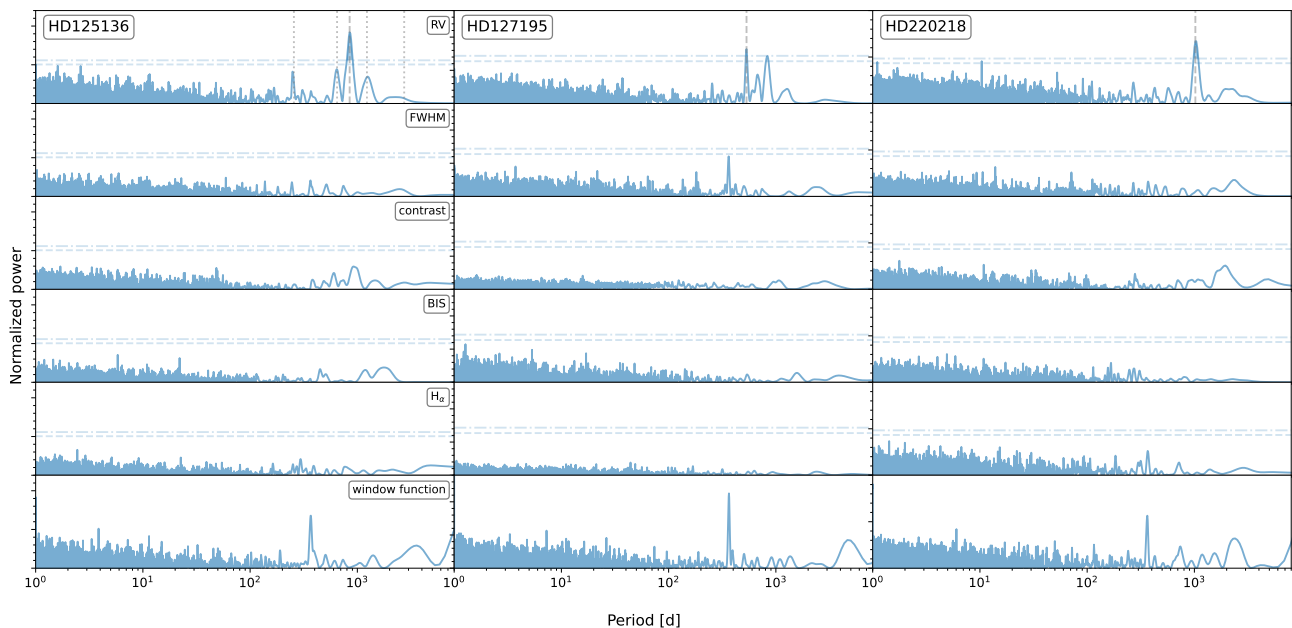


Fig. 3: GLS periodogram of RV, FWHM, contrast, BIS, $H\alpha$, and of the window function (*top to bottom*) for the stars HD 125136 (*left*), HD 127195 (*center*), and HD 220218 (*right*). The FAP levels of 1 and 0.1% are shown as horizontal lines. The highest significance peaks are show as dashed vertical lines and the aliases for HD 125136 are shown as dotted vertical lines.

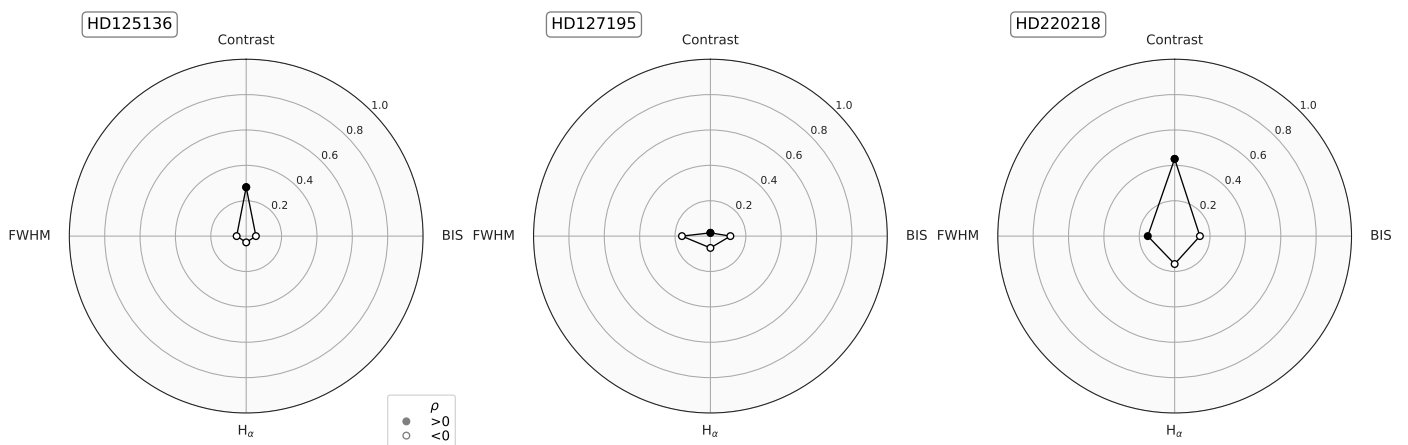


Fig. 4: Radar chart of the correlation between RV and each of the indicators, for the three stars studied in the paper. The filled and open dots representing positive or negative signed Pearson correlation coefficients, respectively.

fixed for the analysis. For each model we obtain at least 50 000 effective samples from the posterior, which allows for a robust sampling of the different parameters.

The classification of a detection with N_p planets as significant depends on the (Keplerian) planet model being favoured relative to the model with N_{p-1} planets, which in turn depends on a chosen metric crossing an a-priori threshold. For exoplanet detection within the Bayesian framework, the metric is typically the Bayes factor, and the threshold of 150, following the “very strong evidence” criterion by Kass & Raftery (1995).

We enforce dynamical stability using the angular momentum deficit criterion (Laskar & Petit 2017) by computing the the angular momentum deficit value for all orbital solutions proposed

by the sampler and assigning zero likelihood to configurations that violate the stability condition. This provides a simple and computationally efficient way to exclude long-term unstable solutions that would still be compatible with the RV data.

Detailed information on priors and posteriors is provided in Appendix C. The choice of priors is discussed in Section C.1 and those adopted are listed in Table C.1. The posterior distribution median values and credible interval are presented in Table 2 and the corner plots presented in Appendix C.2.

Using a Bayes factor threshold of 150, we confidently detect one signal around the stars HD 125136 and HD 220218, and two signals around HD 127195. The phase plots of the maximum a

Table 2: Parameters for the model fitting on the three stars studied in this paper.

Parameter ^a	Unit	HD 125136 b	HD 127195 b	HD 127195 c	HD 220218 b ^b
K	$[\text{m s}^{-1}]$	$36.28^{+2.23}_{-2.26}$	$13.89^{+1.78}_{-1.83}$	$11.56^{+1.73}_{-1.82}$	$27.48^{+4.06}_{-3.77}$
P	[d]	$849.77^{+4.61}_{-4.73}$	$534.50^{+2.85}_{-2.92}$	$836.99^{+9.35}_{-9.67}$	$1034.71^{+17.87}_{-21.19}$
e	–	$0.05^{+0.06}_{-0.04}$	$0.04^{+0.05}_{-0.03}$	$0.05^{+0.05}_{-0.04}$	$0.12^{+0.12}_{-0.09}$
ϕ	$[\circ]$	$3.18^{+1.30}_{-1.54}$	$2.66^{+2.53}_{-1.75}$	$2.83^{+1.51}_{-1.39}$	$4.35^{+0.76}_{-1.29}$
ω		$3.13^{+2.67}_{-2.62}$	$3.10^{+1.97}_{-1.93}$	$4.12^{+1.21}_{-2.43}$	$1.22^{+3.98}_{-0.81}$
Jitter _{COR98}		$10.35^{+13.06}_{-4.14}$	$13.62^{+14.51}_{-6.12}$	–	–
Jitter _{COR07}		$6.33^{+1.72}_{-0.94}$	$7.72^{+2.04}_{-1.47}$	–	$27.57^{+8.95}_{-7.04}$
Jitter _{COR14}		$9.43^{+2.78}_{-2.14}$	$8.01^{+1.52}_{-1.26}$	–	$11.23^{+2.79}_{-2.27}$
Jitter _{COR24}	$[\text{m s}^{-1}]$	–	$11.43^{+6.13}_{-3.56}$	–	$7.83^{+3.54}_{-2.00}$
Offset _{COR07-98}		$5.19^{+14.66}_{-16.64}$	$37.26^{+17.04}_{-21.42}$	–	–
Offset _{COR14-07}		$2.95^{+8.46}_{-8.47}$	$32.26^{+10.60}_{-12.69}$	–	$4.36^{+24.61}_{-25.69}$
Offset _{COR24-14}		–	$18.77^{+6.31}_{-9.28}$	–	$2.87^{+14.42}_{-15.88}$
Slope	$[\text{m s}^{-1}]$	$0.002^{+0.003}_{-0.003}$	$0.003^{+0.002}_{-0.002}$	–	$0.000^{+0.005}_{-0.005}$
v_{sys}		$0.68^{+5.15}_{-5.36}$	$-21.11^{+11.27}_{-7.10}$	–	$0.40^{+18.05}_{-15.78}$

Notes. ^(a) Expected value provided by the median and uncertainties by the 16–84% credible intervals of the posterior distribution. ^(b) Activity-rooted signal; see text for details.

posteriori (MAP) sample models are shown in Figures 5, 6, and 7.

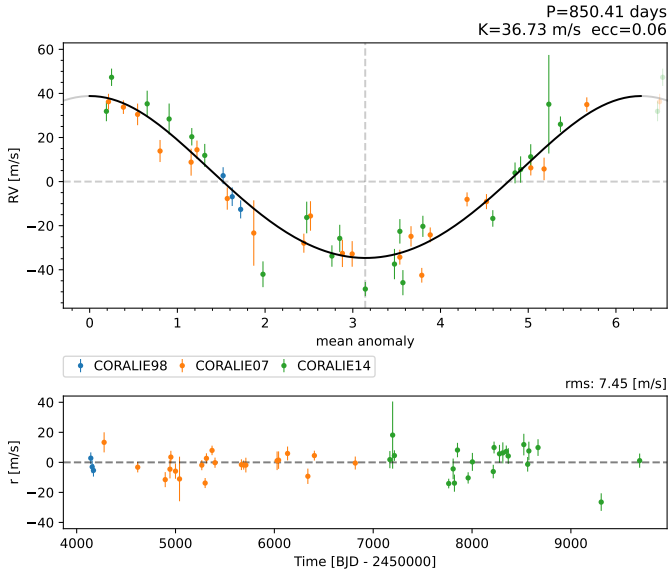


Fig. 5: Phase plot and residuals as a function of mean anomaly for the planet detected around HD 125136.

It is important to notice that the jitter on HD 220218 ($7\text{--}26 \text{ m s}^{-1}$) is noticeably larger than on other stars ($6\text{--}14 \text{ m s}^{-1}$, or $6\text{--}11 \text{ m s}^{-1}$ if we exclude the 3-point dataset of HD 127195). The corner plot for HD 220218 also show that the amplitude of the RV signal K_0 is correlated with other parameters such as the e , ϕ and the jitter term. The fitting of the signal with the current data points and model is thus ambiguous, and we do not interpret the signal as being created by a planetary companion.

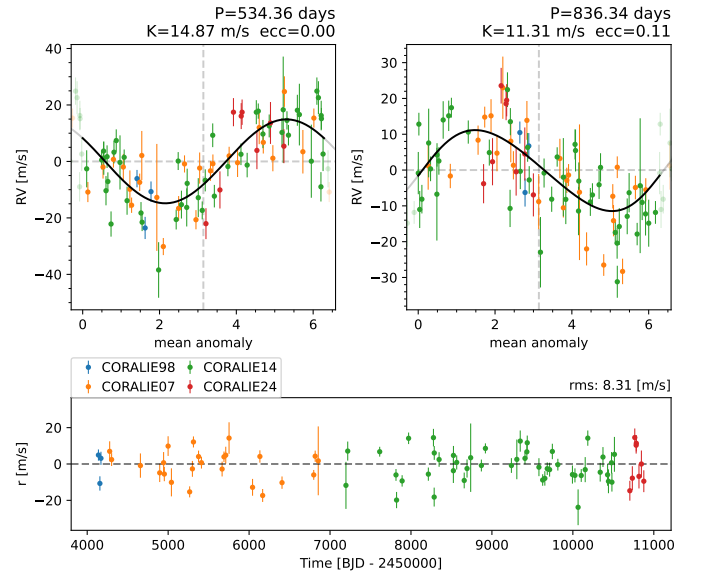


Fig. 6: Phase plot and residuals as a function of mean anomaly for the two planets detected around HD 127195.

4. Sub-Giants Pulsations and achievable RV stability

To estimate the signal introduced by stellar pulsations we used the model described in [Figueira et al. \(2025\)](#). In a nutshell, the stellar parameters mass M , luminosity L , radius R , and effective temperature T_{eff} are used to derive the asteroseismic parameters using robust scaling relations plus reference values calibrated from asteroseismic analyses. These star-tailored values allows us to model the RV signal created by pulsations. The observational campaign on the star is modelled as a sequence of n intra-night

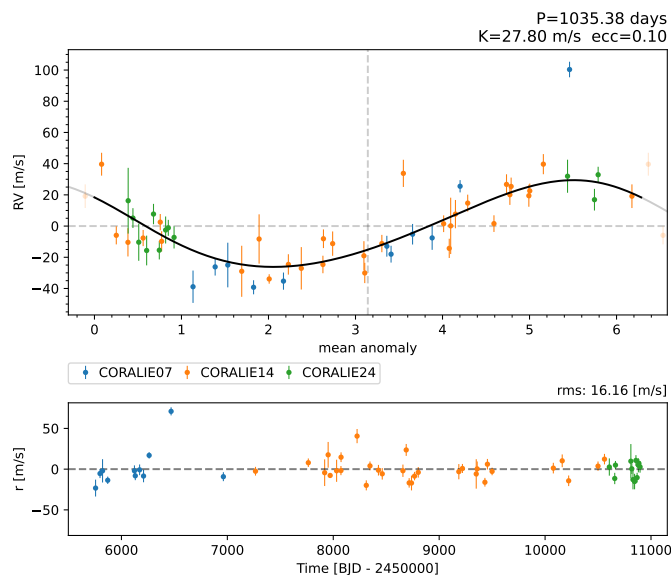


Fig. 7: Phase plot and residuals as a function of mean anomaly for the signal detected around HD 220218.

integrations with a predefined exposure time, a given time gap between exposures and a photon-noise uncertainty. For a time series acquired in this way, the model predicts the nightly averaged RV (when considering photon noise and pulsations), plus the average intra-night scatter. An installable Python package was made available on GitHub⁷.

To test our ability to average out pulsations we selected HD 127195. This star was chosen from among the three studied in this work because it is slightly brighter than HD 125136 (V 7.19 mag vs 7.44 mag), with HD 220218 not being considered for having its RVs dominated by activity.

For HD 127195 we estimate a pulsation envelope amplitude of 0.9 m s^{-1} , populated by 14 modes and a peak period at $\sim 1 \text{ h}$. We tested different observation schemes, and selected three observations of 300 s separated by 1200–1500 s, assuming a photon noise of 4–4.5 m s^{-1} for each individual exposure. In these conditions, the error on the nightly average introduced by the pulsation is expected to be only $\sim 3 \text{ m s}^{-1}$; for comparison, if we used a single integration of 900 s the value would increase to 5 m s^{-1} .

In August 2025 we performed a dedicated observing campaign to emulate this scheme. The star was observed on 7 nights over a timespan of 23 days; overall the observing conditions were good (transparency only reduced by thin clouds, seeing $< 1''$), and the target precision was attained, albeit with some variance. The nightly scatter ranged from 2 to 8 m s^{-1} , very probably due to variable observing conditions, but the median value was 4 m s^{-1} , the expected value from simulations.

To test whether this observing strategy was successful at reducing the RV scatter, we repeated the analysis performed in Sect. 3.3, now including the dataset CORALIE25 composed of the nightly-averaged observations done with the new strategy. The results are presented in Table D.1. The planetary parameters and instrument characterization for the datasets CORALIE98 to CORALIE24 are, within their credible interval, fully compatible with those derived previously. The MAP solution provides both a jitter and an rms of the residuals of 5 m s^{-1} , significantly lower than for the other datasets (see Table D.2, and Fig. D.1). This aligns with our predictions, with a stellar contribution to

the uncertainties of 3 m s^{-1} and an instrumentation stability contribution of 4 m s^{-1} . Conversely, if the instrument stability is of only 3 m s^{-1} , this means our stellar signal is still at 4 m s^{-1} .

To our knowledge, there are only a few cases in which an RV precision below 5 m s^{-1} has been achieved for giant stars. A recent example is the work of Grunblatt et al. (2024) on TIC 365102760, which, through a joint analysis of photometry and RV data, reports a jitter of 4.2 m s^{-1} .

5. Discussion

5.1. Detected signals: planets or stellar activity?

Stellar phenomena can create false positive signals, and some can reach the timescales of hundreds of days we modelled. Radial pulsations are directly excluded from the simulations in Sect. 4 and works such as Cox (1980), which show that pulsation timescales do not exceed $\sim 1 \text{ day}$. Low-luminosity red giant stars have measured surface rotation periods primarily in the range of ~ 10 – 200 d , based on spot-modulation analyses of *Kepler* light curves (e.g. Ceillier et al. 2017; Gaulme et al. 2020), with a detection tail extending toward longer periods but strongly affected by incompleteness. Since only a small fraction of red giant stars exhibit detectable photometric modulation, likely due to weak magnetic activity and finite spot lifetimes, rotation periods longer than $\sim 200 \text{ d}$ may remain undetected in current photometric data. A realistic rotational period estimate can be obtained from stellar evolution models including angular momentum transport in radiative interiors (e.g. Eggenberger et al. 2012; Tayar & Pinsonneault 2013). These models include enhanced angular momentum transport that leads to partial core–envelope coupling, as required by asteroseismic constraints. While a simple scaling based on envelope expansion ($P \propto R^2$) yields an upper bound for rotation periods on the red giant branch $P_{\text{RGB}} \sim 300$ – 500 d when considering a star evolving from the main sequence and associated period $P_{\text{MS}} \sim 20$ – 30 d and reaching $R \sim 4 R_{\odot}$, models including angular momentum transport typically predict surface rotation periods of ~ 30 – 150 d at this evolutionary stage. This range is consistent with forward modelling predictions and suggests that very long periods ($\geq 300 \text{ d}$) are likely associated with weak internal coupling or unusually low initial angular momentum.

The other candidate mechanism is magnetic cycles. Lovis et al. (2011) studied the chromospheric activity in ~ 300 stars over 2–7 yr and concluded that while $61 \pm 8\%$ of FGK main-sequence stars show a magnetic cycle, this number drops to $12 \pm 5\%$ for subgiants. Their results are in line with previous studies that found that stars show lower chromospheric activity as they evolve off the main sequence (e.g. Wright 2004). The work of Gomes da Silva et al. (2021) confirmed this result with a much larger sample, and even showed that the few evolved stars with high chromospheric activity were unusually massive or young, as proposed by Luhn et al. (2020). Lovis et al. (2011) also found that the sensitivity of RV to cycles is almost zero for $T_{\text{eff}} \sim 4800 \text{ K}$, a value very similar to that of our stars. Magnetic cycles are less likely to have a significant impact on RV if present. They cannot be discarded as potential mechanisms generating the measured signals, given that their typical timescales overlap with the observed periodicities.

There is an alternative mechanism worth mentioning. Spaeth et al. (2024) explored the origin of a periodic signal with 674 d measured on the giant star NGC 4349 No. 127. The authors showed that the RV and activity-indicator time series, as well as the correlations between them, were well reproduced by

⁷ <https://github.com/pedrorfigueira/rvpulsim>

non-radial pulsations. Depending on the angular degree l and azimuthal mode m , the correlation with indicators can show very different strengths, being intrinsically low in some cases ($m=0$). The authors were motivated by the work of Saio et al. (2015), who proposed oscillatory convective modes as the mechanism explaining long secondary periods of 200–1500 d measured on the photometry of low-mass red giants. If we extrapolate the period estimations of Saio et al. (2015) to our luminosity domain (or use the empirical rule that long secondary periods have periods of 5–10 times the fundamental radial pulsation) we obtain periods of the order of a few tens of days. So this is unlikely to be an explanation for the observed signals at $P > 500$ d.

Considering the different scenarios, we therefore conclude the signals observed in HD 125136 and HD 127195 are very probably of planetary origin. Our only reservation is that their periods fall within the range of long-term activity cycles, that have weak RV signatures on subgiant stars. The planet around HD 125136 has a minimum mass $m \sin i$ of $2.26 \pm 0.08 M_{\text{Jup}}$ and a period of 850 d; for HD 127195, the planets have minimum masses of $0.67 \pm 0.02 M_{\text{Jup}}$ and $0.65 \pm 0.02 M_{\text{Jup}}$ and have orbital periods of 535 d and 837 d, respectively. The signal detected on HD 220218 shows correlations between the semi-amplitude and other orbital parameters, and is fitted with a jitter much larger than is customary on giant and subgiant stars observed with CORALIE. We consider this a spurious fit, likely driven by stellar activity, and do not discuss it further.

5.2. Planetary orbits through stellar evolutionary phases

To explore the transformation of planetary orbits during stellar evolution we used the framework presented in Esseldeurs et al. (2026). HD 125136 and HD 127195 were simulated as stars with an initial mass of $1.5 M_{\odot}$, and the current time was estimated as the time where the current radius of the star matches the radius of the stellar evolution model. The resulting orbital evolution for HD 125136 b, HD 127195 b and c is shown in Fig. 8.

The planet HD 125136 b will survive the red giant branch (RGB) phase, and due to the mass-loss the planetary orbit will widen during this phase. However, during the asymptotic giant branch (AGB) phase, tides will take over and the planet will spiral inward and be consumed by the star. It will thus not survive until the white dwarf (WD) phase.

The system around HD 127195 will undergo similar evolutionary effects over the same milestones but with a different final outcome. As the star enters the RGB phase, HD 127195 b will experience a slight increase in its semi-major axis due to stellar mass-loss, but will return close to its initial value as tides become important. The duration of the RGB phase is sufficiently short for the planet to survive through it. During the AGB phase however, tides continue to shrink the semi-major axis until it is swallowed by the star, similar to HD 125136 b. On the other hand, as planet c starts on a similar orbit as HD 125136 b, their evolution until the AGB phase will be similar. However, as HD 127195 c has a lower mass, tides will have a weaker impact, allowing mass-loss to widen the orbit and permitting the survival of the planet up to the WD phase.

5.3. RV noise floor for evolved stars and achievable precision

The rms of the residuals on the planetary models is $7\text{--}8 \text{ m s}^{-1}$, in excess of the photon noise of $\sim 5 \text{ m s}^{-1}$. The extra component on the error budget can be due to the instrument or intrinsic stellar

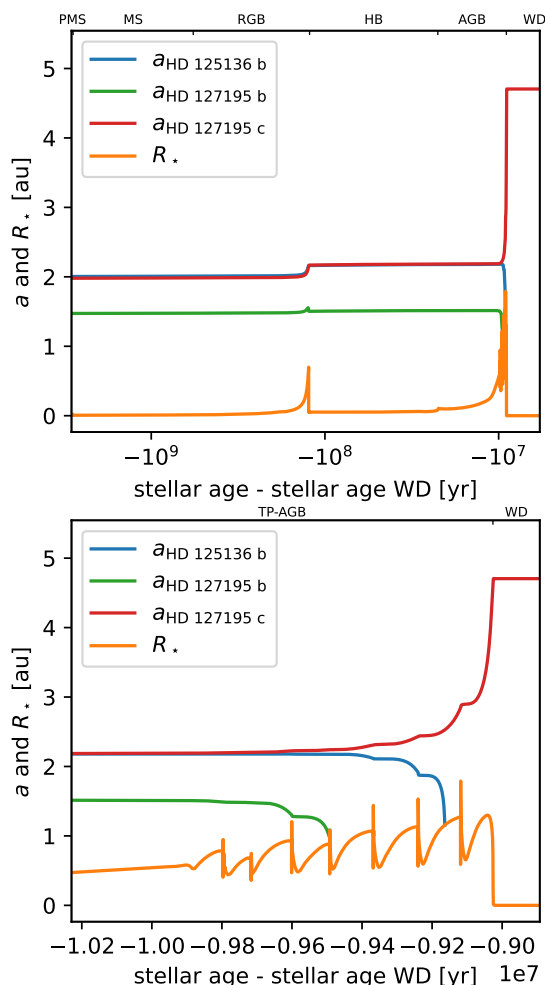


Fig. 8: Semi-major axis of planetary orbit and stellar radius as a function of stellar age for the systems HD 125136 and HD 127195. The orbits of the three planets are presented in different colours; note the R_* is common to the two stars.

RV stability, and the most likely contributor is stellar p-mode oscillations.

Yu et al. (2018) estimated the impact of oscillations on RV of dwarf to giant stars using *Kepler* data and re-fitting scaling relationships. The authors estimated an RV scatter of 1.5 m s^{-1} on subgiants and of 4 m s^{-1} for low-luminosity giants. These values are lower than those measured on subgiant surveys, as presented by Johnson et al. (2010) and Johnson et al. (2011), that estimated the noise floor to be at 5 m s^{-1} when accounting for the various sources of stellar variability.

Luhn et al. (2020) measure a RV jitter of $5\text{--}10 \text{ m s}^{-1}$ for slightly evolved stars (subgiants and low-luminosity giants) with masses similar to those of our targets. The authors also predict the dependence on stellar parameters using a chromospheric term and dividing the convective component into oscillation and granulation. Figueira et al. (2025) showed that the granulation signature of the main sequence chromospherically quiet τ Cet (K0V) is lower than predicted from the Sun; one can speculate that chromospherically quiet K evolved stars also exhibit a reduced granulation component, and thus pulsations become the main engine behind RV variability.

Theoretical works like that Telting & Schrijvers (1997) and observational campaigns like the one reported by Luhn et al.

(2025) on the subgiant HD 142091 showed that pulsation signals present negligible line profile variations and very weak chromatic dependence, making them difficult to distinguish once detected. The results from the observing campaign described in Sect. 4 show this effect can be mitigated efficiently by the observing strategy. The 4 m s^{-1} scatter achieved in this first test encourages applying this strategy at higher photon-noise precision and over longer observing baselines.

5.4. Compatibility limits and detectable planets

When running *kima* one can fix the parameter N_p to the number of detected planets plus one to estimate the parameters of undetected planets that are compatible with the data (see Standing et al. 2022). The samples with the largest semi-amplitude K_0 for a given period bin correspond to the most massive planet compatible with the data and the adopted priors. The compatibility limits produced in this way are, by construction, marginalized over all parameters other than mass and period. In these simulations, we set as stellar masses the values presented in Ottoni et al. (2022), listed in Table A.2. We present the compatibility limits in Fig. 9.

The compatibility limits show that we are confidently able to detect planets with an amplitude larger than 10 m s^{-1} . This is in excess of the $\sim 5 \text{ m s}^{-1}$ of precision of CORALIE and photon-noise uncertainty of our measurements, but in line with the expectations that subgiant stars have an additional source of noise up to $\sim 10 \text{ m s}^{-1}$ (see previous section). We are able to detect planets with roughly twice the mass of Neptune on short orbits of $\sim 10 \text{ d}$ and Saturn-mass planets up to 100 d . On some stars we can detect Jupiter-mass planets with orbit periods up to $\sim 1000 \text{ d}$, but for others only planets with more than twice the mass of Jupiter are detectable. The values will depend on the characteristics of star and of the observations, but the cases studied here provide representative order-of-magnitude estimates.

5.5. Demographics of planets around evolved stars

Dedicated RV surveys have measured the occurrence rate of planets around evolved stars (Reffert et al. 2015; Ghezzi et al. 2018), with Wolthoff et al. (2022) pooling together different surveys. Today we know that giant-planet occurrence rises with stellar mass from $\leq 1 M_\odot$ up to $1.7\text{--}1.9 M_\odot$ (with a peak occurrence of $10\text{--}20\%$ in this mass domain), decreasing very sharply for higher mass hosts. The difference in occurrence rates reported by different surveys can be explained by different choices in sample selection and completeness corrections. Wolthoff et al. (2022) performed the most homogeneous analysis and reaches an overall giant planet occurrence of 10.7% that peaks at $1.68 \pm 0.59 M_\odot$. Interestingly, the authors also found that the period distribution for detected giants peaks at $700\text{--}800 \text{ d}$ where the occurrence is higher than reported for main-sequence FGK samples, a result already presented by Reffert et al. (2015) for comparable periods and masses. Although this higher occurrence is expected to be real (the authors carefully accounted for observational biases), there is always the possibility of false positives, as shown recently by Hatzes et al. (2025).

In Fig. 10 we represent the planets currently known to orbit stars with a mass above $1.1 M_\odot$. This corresponds to $\sim 21\%$ of the planets known, with the percentage being reduced to $\sim 11\%$ when restricting the sample to planets with masses measured via RV. The planets presented in this work fall close to this occurrence $700\text{--}800 \text{ d}$ peak in period space, yet they are in an

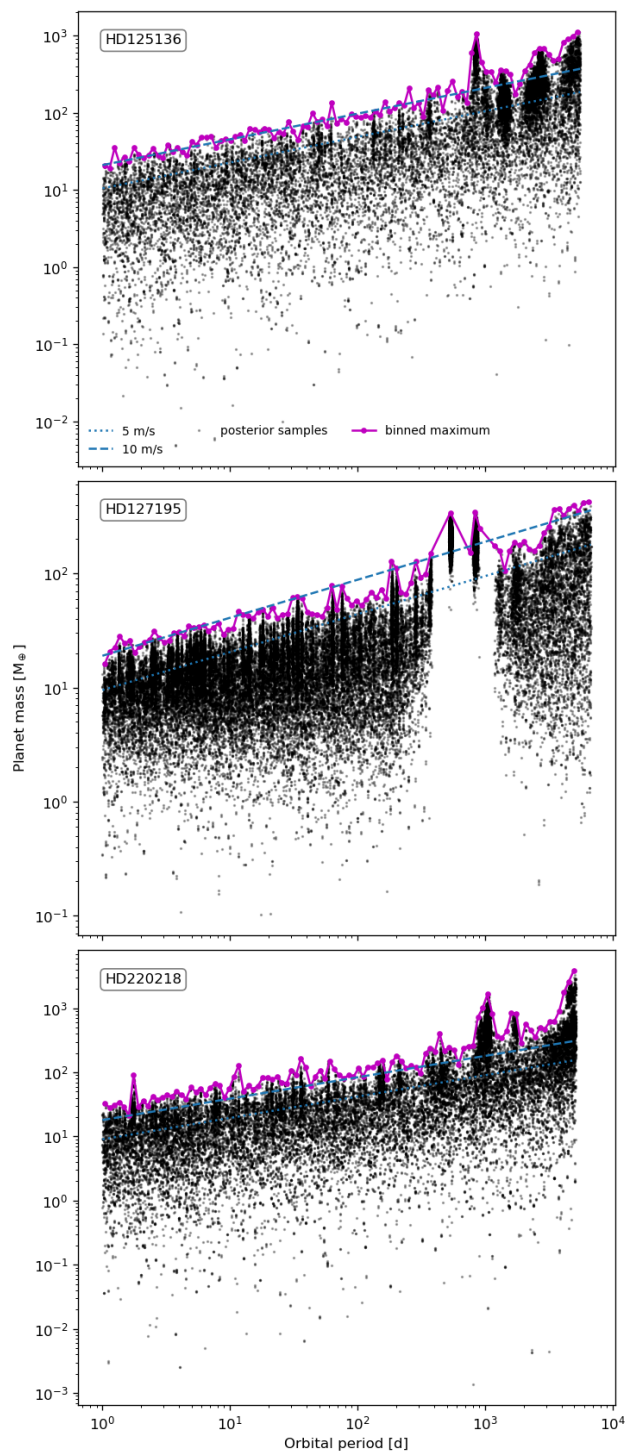


Fig. 9: Compatibility limits for the three stars studied, HD 125136 (top), HD 127195 (middle), and HD 220218 (bottom). The maximum RV amplitude of the samples is plotted along with lines corresponding to a mass with amplitude equal to a precision limit of 5 and 10 m s^{-1} .

area that remains sparsely populated. The diagram is a stark reminder of how hard it is to follow stars for timescales of decades with stable RV spectrographs. While we know that giant planets have higher occurrence rates around giant-stars and sub-Neptunes around M-dwarfs (see e.g. review by Mulders 2018) and that giant planet occurrence peaks near the snow line (e.g. Fernandes et al. 2019), it remains unclear whether the apparent

dearth of Neptune-mass planets at comparable separations is a consequence of detection bias or a direct outcome of planet formation.

Transit surveys, which are primarily sensitive to short-period systems, provide very different yet complementary constraints on the occurrence of planets around evolved stars. The studies of Grunblatt et al. (2019) and Temmink & Snellen (2023) used *Kepler* and TESS data, respectively, to evaluate the occurrence rate of short-period giant planets and compare the results with the values obtained around main-sequence stars. The occurrence rates remained compatible, suggesting that the effects of stellar evolution on the tidal decay and engulfment of Jupiter-mass close-in ($P < 10$ d) planets are not significant until stars leave the low-luminosity giant branch regime. However, the more recent work of Bryant & Van Eylen (2025) characterized a larger number of stars and determined more precise occurrence rates. The study measured a significant decrease between sub-giants and low-luminosity giants, and of these compared with main sequence planets, with a larger occurrence rate decrease measured for shorter planets. This provided clear evidence that the population of short-period giant planets is being sculpted by the post-main-sequence evolution of the host stars, as discussed for our longer-period planets in Section 5.2.

6. Conclusions

We analysed data acquired with the CORALIE spectrograph in the context of the survey CASCADES on three subgiant stars: HD 125136, HD 127195, and HD 220218. The RV time series, spanning 15–18 yr, revealed the presence of several stellar signals. We interpret the signal on HD 125136 as created by a planet with a minimum mass of $2.26 \pm 0.08 M_{\text{Jup}}$ and a period of 850 d. On HD 127195 we detect a two-planet system, with the planets having a minimum mass of $0.67 \pm 0.02 M_{\text{Jup}}$ and $0.65 \pm 0.02 M_{\text{Jup}}$ with orbital periods of 535 d and 837 d, respectively. There is no correlation between RV and activity indicators timeseries and the latter do not show any significant periodicity. However, one cannot fully exclude that these signals are false positives, in particular created by long-term magnetic cycles. The signal around HD 220218 is interpreted as spurious, and very likely caused by stellar activity.

The three planets around HD 125136 and HD 127195 fall on a parameter space poorly populated in stellar mass and period. The systems reported here therefore provide useful constraints on the population of Saturn and Jupiter planets around evolved stars. We showed that on the subgiant HD 127195 a dedicated observing strategy can efficiently average out stellar pulsations to below 5 m s^{-1} . Such strategies will be increasingly important for extending RV planet searches to evolved stars with higher intrinsic variability.

Data availability

The RV data for the targets discussed in this work are available in electronic form at the CDS via anonymous ftp to [cdsarc.u-strasbg.fr](ftp://cdsarc.u-strasbg.fr) (130.79.128.5) or via <http://cdsweb.u-strasbg.fr/cgi-bin/qcat?J/A+A/>. The CORALIE data, reduced with the latest version of the pipeline, can also be accessed through the DACE platform via <https://doi.org/10.82180/dace-3js7g119>. to update upon acceptance.

Acknowledgements. We thank the anonymous referee for insightful and very valuable comments on the first version of the manuscript. Based on obser-

vations collected with CORALIE echelle spectrograph mounted on the Euler 1.2 m Swiss telescope at La Silla, Chile. PF thanks P. Eggenberger for very interesting discussions on stellar pulsations. PF acknowledges support from the COST Action CA22133 PLANETS. PF and RL acknowledges financial support from the Severo Ochoa grant CEX2021-001131-S funded by MCIN/AEI/10.13039/501100011033. PF is also funded by the European Union (ERC, THIRSTEE, 101164189). Views and opinions expressed are however those of the author(s) only and do not necessarily reflect those of the European Union or the European Research Council. Neither the European Union nor the granting authority can be held responsible for them. ME acknowledges support from the FWO grants G0B3823N and G099720N. MS thanks the Belgian Federal Science Policy Office (BELSPO) for the provision of financial support in the framework of the PRODEX Programme of the European Space Agency (ESA) under contract number C4000140754. This work has made use of data from the European Space Agency (ESA) mission *Gaia* (<https://www.cosmos.esa.int/gaia>), processed by the *Gaia* Data Processing and Analysis Consortium (DPAC, <https://www.cosmos.esa.int/web/gaia/dpac/consortium>). Funding for the DPAC has been provided by national institutions, in particular the institutions participating in the *Gaia* Multilateral Agreement. This work made use of *astropy*, a community-developed core Python package and an ecosystem of tools and resources for astronomy, described in *astropy collaboration* (2013), *astropy collaboration* (2018), and *astropy collaboration* (2022). Corner plots were created using the package *corner.py*, described in Foreman-Mackey (2016).

References

- Alibert, Y., Mordasini, C., & Benz, W. 2011, *A&A*, 526, A63
 Alibert, Y., Mordasini, C., Benz, W., & Winisdoerffer, C. 2005, *A&A*, 434, 343
 Allard, F., Homeier, D., & Freytag, B. 2012, *Philosophical Transactions of the Royal Society of London Series A*, 370, 2765
 Baluev, R. V. 2008, *MNRAS*, 385, 1279
 Baranne, A., Queloz, D., Mayor, M., et al. 1996, *A&AS*, 119, 373
 Boisse, I., Moutou, C., Vidal-Madjar, A., et al. 2009, *A&A*, 495, 959
 Borgniet, S., Lagrange, A. M., Meunier, N., et al. 2019, *A&A*, 621, A87
 Brewer, B. J. 2014, arXiv e-prints, arXiv:1411.3921
 Brewer, B. J., Pártay, L. B., & Csányi, G. 2009, arXiv e-prints, arXiv:0912.2380
 Bryant, E. M. & Van Eylen, V. 2025, *MNRAS*, 544, 1186
 Buldgen, G., Ottoni, G., Pezzotti, C., et al. 2022, *A&A*, 657, A88
 Castelli, F. & Kurucz, R. L. 2003, in *Modelling of Stellar Atmospheres*, ed. N. Piskunov, W. W. Weiss, & D. F. Gray, Vol. 210, A20
 Ceillier, T., Tayar, J., Mathur, S., et al. 2017, *A&A*, 605, A111
 Cincunegui, C., Díaz, R. F., & Mauas, P. J. D. 2007, *A&A*, 469, 309
 Cox, J. P. 1980, *Theory of Stellar Pulsation*, Princeton Series in Astrophysics (Princeton, NJ: Princeton University Press)
 Creevey, O. L., Sordo, R., Pailler, F., et al. 2023, *A&A*, 674, A26
 Eggenberger, P., Haemmerlé, L., Meynet, G., & Maeder, A. 2012, *A&A*, 539, A70
 Esseldeurs, M., Decin, L., De Ridder, J., et al. 2026, *Nature Astronomy*, 10, 124
 Faria, J. P., Santos, N. C., Figueira, P., & Brewer, B. J. 2018, *The Journal of Open Source Software*, 3, 487
 Fernandes, R. B., Mulders, G. D., Pascucci, I., Mordasini, C., & Emsenhuber, A. 2019, *ApJ*, 874, 81
 Feroz, F., Balan, S. T., & Hobson, M. P. 2011, *MNRAS*, 415, 3462
 Figueira, P., Faria, J. P., Silva, A. M., et al. 2025, *A&A*, 700, A174
 Figueira, P., Santos, N. C., Pepe, F., Lovis, C., & Nardetto, N. 2013, *A&A*, 557, A93
 Fontanet, E., Udry, S., Ségransan, D., et al. 2025, *A&A*, 699, A38
 Fuhrmann, K. 1998, *A&A*, 338, 161
 Fulton, B. J., Petigura, E. A., Howard, A. W., et al. 2017, *AJ*, 154, 109
 Gaia Collaboration, Prusti, T., de Bruijne, J. H. J., et al. 2016, *A&A*, 595, A1
 Gaia Collaboration, Vallenari, A., Brown, A. G. A., et al. 2023, *A&A*, 674, A1
 Gaulme, P., Jackiewicz, J., Spada, F., et al. 2020, *A&A*, 639, A63
 Ghezzi, L., Montet, B. T., & Johnson, J. A. 2018, *ApJ*, 860, 109
 Ginsburg, A., Sipőcz, B. M., Brasseur, C. E., et al. 2019, *AJ*, 157, 98
 Gomes da Silva, J., Santos, N. C., Adibekyan, V., et al. 2021, *A&A*, 646, A77
 Gregory, P. C. 2005, *ApJ*, 631, 1198
 Grunblatt, S. K., Huber, D., Gaidos, E., et al. 2019, *AJ*, 158, 227
 Grunblatt, S. K., Saunders, N., Huber, D., et al. 2024, *AJ*, 168, 1
 Hatzes, A. P., Perdelwitz, V., Karjalainen, M., et al. 2025, *A&A*, 699, A260
 Husser, T. O., Wende-von Berg, S., Dreizler, S., et al. 2013, *A&A*, 553, A6
 Johnson, J. A., Clanton, C., Howard, A. W., et al. 2011, *ApJS*, 197, 26
 Johnson, J. A., Fischer, D. A., Marcy, G. W., et al. 2007, *ApJ*, 665, 785
 Johnson, J. A., Howard, A. W., Bowler, B. P., et al. 2010, *PASP*, 122, 701
 Kass, R. E. & Raftery, A. E. 1995, *Journal of the American Statistical Association*, 90, 773
 Kennedy, G. M. & Kenyon, S. J. 2008, *ApJ*, 673, 502
 Kipping, D. M. 2013, *MNRAS*, 434, L51

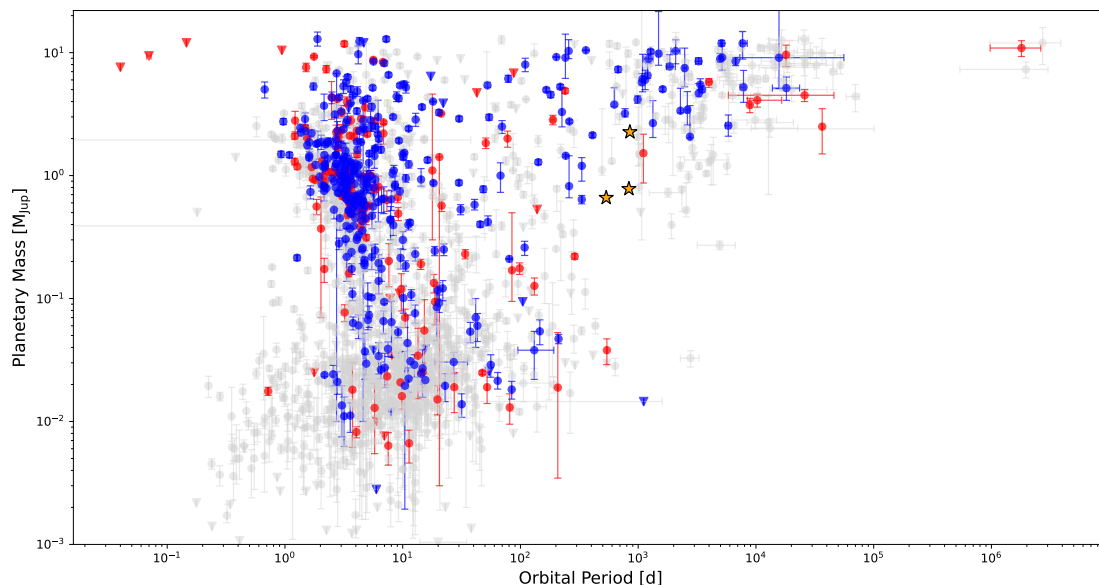


Fig. 10: Mass-Period diagram for RV-characterized exoplanets (*blue*) or with other methods (*red*) around hosts with mass $M_* > 1.1 M_\odot$, when compared with other known planets (*grey*). Only objects with planetary mass $m < 13 M_{\text{Jup}}$ are considered; mass upper limits are marked with inverted triangles. The three planets presented in this paper are represented as orange stars.

- Kumaraswamy, P. 1980, *Journal of Hydrology*, 46, 79
- Kurucz, R. L. 1993, Kurucz CD-ROM, Vol. 18, SYNTHE spectrum synthesis programs and line data (Cambridge, MA: Smithsonian Astrophysical Observatory)
- Laskar, J. & Petit, A. C. 2017, *A&A*, 605, A72
- Louis, C., Dumusque, X., Santos, N. C., et al. 2011, arXiv e-prints, arXiv:1107.5325
- Louis, C. & Mayor, M. 2007, *A&A*, 472, 657
- Luhn, J. K., Robertson, P., Halverson, S., et al. 2025, *ApJ*, 987, 168
- Luhn, J. K., Wright, J. T., Howard, A. W., & Isaacson, H. 2020, *AJ*, 159, 235
- Mayor, M. & Queloz, D. 1995, *Nature*, 378, 355
- McNally, D. 1965, *The Observatory*, 85, 166
- Mulders, G. D. 2018, in *Handbook of Exoplanets*, ed. H. J. Deeg & J. A. Belmonte, 153
- Otonari, G., Udry, S., Ségransan, D., et al. 2022, *A&A*, 657, A87
- Pepe, F., Mayor, M., Galland, F., et al. 2002, *A&A*, 388, 632
- Pezzotti, C., Otonari, G., Buldgen, G., et al. 2022, *A&A*, 657, A89
- Queloz, D., Henry, G. W., Sivan, J. P., et al. 2001, *A&A*, 379, 279
- Queloz, D., Mayor, M., Weber, L., et al. 2000, *A&A*, 354, 99
- Reffert, S., Bergmann, C., Quirrenbach, A., Trifonov, T., & Künstler, A. 2015, *A&A*, 574, A116
- Saio, H., Wood, P. R., Takayama, M., & Ita, Y. 2015, *MNRAS*, 452, 3863
- Ségransan, D., Udry, S., Mayor, M., et al. 2010, *A&A*, 511, A45
- Spaeth, D., Reffert, S., Hunt, E. L., Kaminski, A., & Quirrenbach, A. 2024, *A&A*, 689, A91
- Standing, M. R., Triaud, A. H. M. J., Faria, J. P., et al. 2022, *MNRAS*, 511, 3571
- Takeda, Y., Ohkubo, M., Sato, B., Kambe, E., & Sadakane, K. 2005, *PASJ*, 57, 27
- Tayar, J., Claytor, Z. R., Huber, D., & van Saders, J. 2022, *ApJ*, 927, 31
- Tayar, J. & Pinsonneault, M. H. 2013, *ApJ*, 775, L1
- Telting, J. H. & Schrijvers, C. 1997, *A&A*, 317, 723
- Temmink, M. & Snellen, I. A. G. 2023, *A&A*, 670, A26
- Van Eylen, V., Agentoft, C., Lundkvist, M. S., et al. 2018, *MNRAS*, 479, 4786
- VanderPlas, J. T. 2018, *ApJS*, 236, 16
- Venturini, J., Ronco, M. P., Guilera, O. M., et al. 2024, *A&A*, 686, L9
- Vines, J. I. & Jenkins, J. S. 2022, *MNRAS*, 513, 2719
- Wittenmyer, R. A., Endl, M., Wang, L., et al. 2011, *ApJ*, 743, 184
- Wolthoff, V., Reffert, S., Quirrenbach, A., et al. 2022, *A&A*, 661, A63
- Wright, J. T. 2004, *AJ*, 128, 1273
- Yu, J., Huber, D., Bedding, T. R., & Stello, D. 2018, *MNRAS*, 480, L48
- Zechmeister, M. & Kürster, M. 2009, *A&A*, 496, 577

Table A.1: ARIADNE input photometry fetched for HD125136, HD127195, and HD220218[†].

Filter	HD125136	HD127195	HD220218
GALEX NUV	15.2180±0.0090	...	15.4240±0.0140
Strömgren <i>u</i>	10.4260±0.0000	...	10.8670±0.0000
Strömgren <i>v</i>	9.0330±0.0000	...	9.5560±0.0000
Tycho <i>B_T</i>	8.6950±0.0160	8.4040±0.0160	9.2200±0.0170
Johnson <i>B</i>	8.4180±0.0100	8.1330±0.0100	8.9840±0.0140
Strömgren <i>b</i>	8.0450±0.0000	...	8.6640±0.0000
<i>Gaia</i> DR3 <i>G_{BP}</i>	7.6689±0.0028	7.4116±0.0028	8.3037±0.0028
Tycho <i>V_T</i>	7.5490±0.0100	7.3000±0.0100	8.1660±0.0110
Strömgren <i>y</i>	7.4400±0.0000	...	8.0840±0.0000
Johnson <i>V</i>	7.4330±0.0080	7.1840±0.0070	8.0620±0.0080
<i>Gaia</i> DR3 <i>G</i>	7.1869±0.0028	6.9385±0.0028	7.8373±0.0028
TESS	6.5875±0.0060	6.3478±0.0060	7.2539±0.0060
<i>Gaia</i> DR3 <i>G_{RP}</i>	6.5385±0.0038	6.2965±0.0038	7.2004±0.0038
2MASS <i>J</i>	5.7610±0.0190	...	6.4380±0.0240
2MASS <i>H</i>	5.2700±0.0440	5.0840±0.0180	5.9450±0.0260
2MASS <i>K_s</i>	5.1440±0.0200	4.9140±0.0210	5.8320±0.0200

Notes. ^(†) The *Gaia* DR3 ids for HD 125136, HD 127195, HD 220218 are 5797485811232714112, 6091942515572349312, and 6490287572484640896, respectively.

Appendix A: Stellar Characterisation

A.1. *Gaia* DR3 data

We used the *astroquery*⁸ package (Ginsburg et al. 2019) to download the *Gaia* data on our targets, complementing it with targets of the solar neighbourhood for illustrative purposes (Fig 1). On top of the GPS-PHOT model that delivers parameters from SED fitting, we select stellar Luminosity, mass, radius and log *g* from the FLAME package, designed to provide reliable estimates for evolved stars. These use evolutionary models, capturing post-MS changes to avoid photometric degeneracies and ensure consistent modelling (Creevey et al. 2023).

A.2. ARIADNE parameters derivation

We used the ARIADNE⁹ package described in Vines & Jenkins (2022) to fetch photometric data of our targets from public surveys and perform Spectral Energy Distribution (SED) fitting of stellar models. The photometry for the three stars is presented on Table A.1.

The program fits the SED across the fetched photometric bands and uncertainties using several stellar atmosphere models and employing Bayesian Model Averaging (BMA). For each star, the final parameter posterior is created by drawing from the posterior of the different models, weighted by their evidence. Model averaging is done over PHOENIX (Husser et al. 2013), BT-Settl (Allard et al. 2012), ATLAS9 (Castelli & Kurucz 2003), and SYNTHE Kurucz (Kurucz 1993) models. ARIADNE then queries *Gaia* DR3 for parameters, and provides the best estimate for several other stellar parameters. We use the default (weakly informative) priors on the parameters to fit. Extinction is fitted using the dustmap SFD from the package *dustmaps*¹⁰.

⁸ <https://astroquery.readthedocs.io/>

⁹ <https://github.com/jvines/astroARIADNE>

¹⁰ <https://dustmaps.readthedocs.io/en/latest/maps.htm>

A.3. Comparison between CASCADES, *Gaia* DR3 and ARIADNE data

The best-fit stellar parameters T_{eff} , log *g*, [Fe/H], distance *d*, luminosity *L*, radius *R*, mass *M* and Age are presented on Table A.2 and represented graphically in Fig A.1.

ARIADNE seems to overestimate log *g* when compared with the other two datasets. The T_{eff} , luminosity and mass for HD 220218 from *Gaia* DR3 are significantly larger than those derived with the other methods. Finally, the *Gaia* formal uncertainties on T_{eff} and log *g* are much smaller than 1%, and as a consequence we are certainly limited by the method's accuracy, as discussed in Tayar et al. (2022).

Appendix B: CORALIE files header keywords used for quality control

The CORALIE fits files contain a large number of automatically generated keywords, of which several are particularly useful for quality control:

- HIERARCH ESO DRS DRIFT QC: quality control flag for the simultaneous drift calculation; PASSED if the drift is successfully measured and its absolute value is below 110 m s⁻¹, otherwise FAILED.
- HIERARCH ESO OBS MOON SEP - angular separation, in degrees, between the Moon and the target on the sky (approximate value, computed at the middle of the night).
- HIERARCH ESO OBS TARG VPICMOON - difference, in km s⁻¹, between the RV of the Sun as reflected on the Moon and the (user-provided) approximate RV of the target star.

The DRIFT QC includes two different conditions. First, it indicates whether the drift calculation was successful, with the data satisfying a number of internal quality criteria (e.g. flux thresholds and algorithmic convergence). Second, it ensures that the absolute value of the measured drift is smaller than 110 m s⁻¹. The drift correction relies on a first-order approximation of variations in the wavelength solution, which is valid only for small perturbations. An empirical analysis of drift amplitudes and correction performance shows that this approximation remains valid below a threshold of 110 m s⁻¹. Above this value, the correction becomes unreliable and inflates the RV uncertainties in a manner that is difficult to quantify, in which case a new wavelength solution is required.

The MOON SEP keyword represents the angular separation between the target and the Moon on the sky and is used to assess the risk of moonlight contamination of the spectra. Such contamination is expected to be significant only for separations smaller than ~30°, a condition that is not met for our observations. The TARG VPICMOON keyword measures the expected velocity separation between the lunar contamination spectrum and the stellar spectrum and is used to evaluate whether moonlight contamination may significantly affect the measured RVs.

Appendix C: kima analysis

C.1. Parameter priors

We use weakly informative priors as much as possible, using only information derived from simple summary statistics of the data.

The modified log-uniform distribution is a log-uniform distribution with parameters knee *a* and upper limit *b* (Gregory

Table A.2: Comparison of stellar parameters from CASCADES, *Gaia*, and ARIADNE.

Parameter	Method	HD 125136	HD 127195	HD 220218
T_{eff} [K]	CASCADES	4959 ± 34	4981 ± 26	4962 ± 27
	<i>Gaia</i>	$4968.4^{+1.2}_{-1.0}$	$5062.2^{+1.7}_{-1.5}$	$5174.3^{+3.2}_{-2.9}$
	ARIADNE	$4928.20^{+53.34}_{-45.87}$	$5080.98^{+119.04}_{-111.83}$	$4966.95^{+41.22}_{-41.22}$
[Fe/H]	CASCADES	0.02 ± 0.03	-0.04 ± 0.02	-0.17 ± 0.02
	ARIADNE	$0.08^{+0.13}_{-0.10}$	$-0.13^{+0.17}_{-0.17}$	$-0.08^{+0.10}_{-0.11}$
$\log g$	CASCADES	3.11 ± 0.07	3.29 ± 0.08	3.16 ± 0.08
	<i>Gaia</i>	$3.1090^{+0.0016}_{-0.0015}$	$3.3279^{+0.0026}_{-0.0037}$	$3.2567^{+0.0025}_{-0.0027}$
	ARIADNE	$4.07^{+0.41}_{-0.34}$	$4.26^{+0.46}_{-0.39}$	$4.16^{+0.43}_{-0.40}$
d [pc]	CASCADES	121.3 ± 0.4	84.7 ± 0.6	147.6 ± 0.7
	<i>Gaia</i>	$119.97^{+0.20}_{-0.20}$	$83.93^{+0.35}_{-0.23}$	$145.09^{+0.45}_{-0.42}$
	ARIADNE	$121.21^{+0.34}_{-0.20}$	$84.43^{+0.37}_{-0.29}$	$148.76^{+0.94}_{-0.55}$
L [L_{\odot}]	CASCADES	15.80 ± 0.28	9.61 ± 0.19	13.18 ± 0.24
	<i>Gaia</i>	$17.46^{+0.06}_{-0.06}$	$10.92^{+0.05}_{-0.05}$	$15.23^{+0.09}_{-0.09}$
	ARIADNE	$16.89^{+1.00}_{-0.88}$	$10.65^{+1.25}_{-1.05}$	$13.63^{+0.71}_{-0.76}$
M [M_{\odot}]	CASCADES	1.55 ± 0.08	1.34 ± 0.06	1.24 ± 0.05
	<i>Gaia</i>	...	$1.60^{+0.04}_{-0.04}$	$1.85^{+0.04}_{-0.05}$
	ARIADNE	$1.27^{+0.35}_{-0.24}$	$1.39^{+0.28}_{-0.32}$	$1.24^{+0.27}_{-0.22}$
R [R_{\odot}]	CASCADES	5.39 ± 0.09	4.16 ± 0.06	4.91 ± 0.07
	<i>Gaia</i>	$5.64^{+0.11}_{-0.11}$	$4.30^{+0.09}_{-0.09}$	$4.86^{+0.10}_{-0.10}$
	ARIADNE	$5.64^{+0.10}_{-0.11}$	$4.21^{+0.14}_{-0.11}$	$4.98^{+0.11}_{-0.10}$
Age [Gyr]	<i>Gaia</i>	...	$2.3^{+0.2}_{-0.3}$	$1.5^{+0.2}_{-0.2}$
	ARIADNE	$4.03^{+2.36}_{-2.65}$	$2.34^{+2.61}_{-0.978}$	$3.99^{+2.69}_{-2.02}$

2005). Using the modified version allows us to extend the prior to zero, assigning a constant non-zero probability to values below the knee value. For the planet semi-amplitude we use a modified log-uniform prior with a knee at 5 m s^{-1} and an upper limit of 200 m s^{-1} .

For the period we use a log-uniform prior from 1 to 5000 d. The eccentricity is represented with a Kumaraswamy (1980) distribution which is an approximation to the β distribution proposed in Kipping (2013). For the mean anomaly and argument of periastron we use uniform distributions between 0 and 2π .

For the stellar systemic RV and the instrument-related parameters we derive the priors from the datasets: the systemic RV is taken from a uniform distribution between the RV extreme values, and the jitter from a uniform distribution between 5 m s^{-1} to 50 m s^{-1} . The offset is drawn from a uniform distribution between minus and plus the RV span. The linear and quadratic slopes are zero-centred normal distributions with a standard deviation set by the data dispersion.

All priors are listed in Table C.1.

Table C.1: Priors used in the kima analysis.

Group	Parameter	Prior	units
Planet	K_p	$\mathcal{MLU}(5, 200)$	m s^{-1}
	P	$\mathcal{LU}(1.0, \Delta t)$	d
	e	$\mathcal{K}(0.867, 3.03)$	–
	ϕ, ω	$\mathcal{U}(0, 2\pi)$	–
Instruments	Jitter	$\mathcal{U}(0.05, 5)$	m s^{-1}
	Offset	$\mathcal{U}(-\Delta RV, \Delta RV)$	
Star	Linear slope	$\mathcal{N}(0, 10 \frac{\Delta RV}{\Delta r})$	
	Quadratic slope	$\mathcal{N}(0, 10 \frac{\Delta RV}{\Delta r^2})$	m s^{-1}
	Systemic RV	$\mathcal{U}(RV_{\text{min}}, RV_{\text{max}})$	

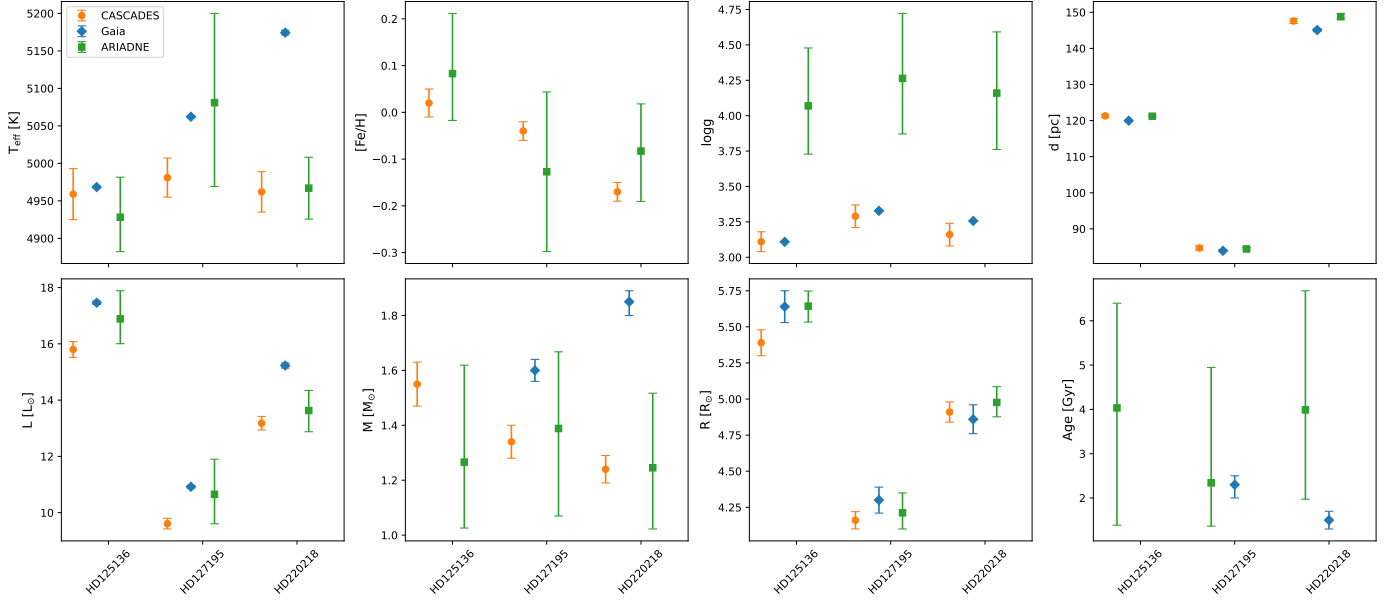


Fig. A.1: Graphical representation of stellar parameters for the three stars and the three determinations methods discussed.

Table D.1: Parameters for the oscillation-averaging campaign on HD 127195.

Parameter [†]	Unit	HD 127195 b	HD 127195 c
K	$[m s^{-1}]$	$13.73^{+1.89}_{-1.98}$	$11.61^{+1.75}_{-1.87}$
P	[d]	$533.71^{+3.14}_{-3.04}$	$835.60^{+10.07}_{-9.96}$
e	–	$0.04^{+0.05}_{-0.03}$	$0.05^{+0.05}_{-0.04}$
ϕ	[°]	$2.69^{+2.60}_{-1.86}$	$2.92^{+1.62}_{-1.56}$
ω		$3.31^{+1.82}_{-2.02}$	$4.04^{+1.34}_{-2.58}$
jitter _{COR98}		$14.19^{+15.24}_{-6.54}$	
jitter _{COR07}		$7.88^{+2.06}_{-1.51}$	
jitter _{COR14}		$8.17^{+1.53}_{-1.25}$	
jitter _{COR24}	$[m s^{-1}]$	$11.40^{+5.77}_{-3.48}$	
jitter _{COR25}		$7.34^{+3.77}_{-1.70}$	
offset _{COR07-98}		$31.94^{+17.52}_{-20.07}$	
offset _{COR14-07}		$29.57^{+8.61}_{-13.52}$	
offset _{COR24-14}		$16.32^{+7.41}_{-8.26}$	
offset _{COR25-24}		$-3.11^{+7.49}_{-7.59}$	
slope		$0.002^{+0.002}_{-0.002}$	
vsys	$[m s^{-1}]$	$-18.39^{+10.56}_{-7.80}$	

Notes. ^(†) Expected value provided by the median and uncertainties by the 16–84% credible intervals of the posterior distribution.

Table D.2: Residual rms and inferred jitter per instrument for the 2025 campaign (values from the MAP solution).

Instrument	rms	jitter
		$[m s^{-1}]$
COR98	6.97	8.51
COR07	8.40	7.15
COR14	8.76	6.78
COR24	10.31	10.52
COR25	5.62	5.07

C.2. Corner plots

Appendix D: Pulsation campaign

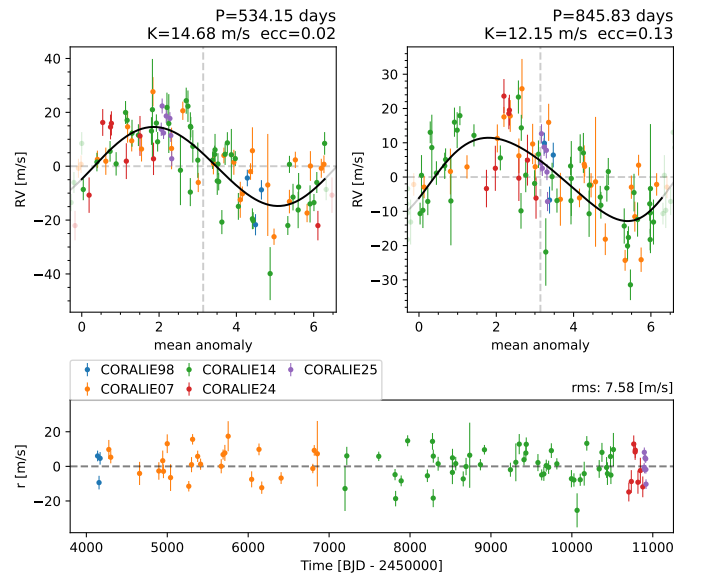


Fig. D.1: Phase plot and residuals as a function of mean anomaly for the two planets detected around HD 127195 when using pulsation-reducing campaign.

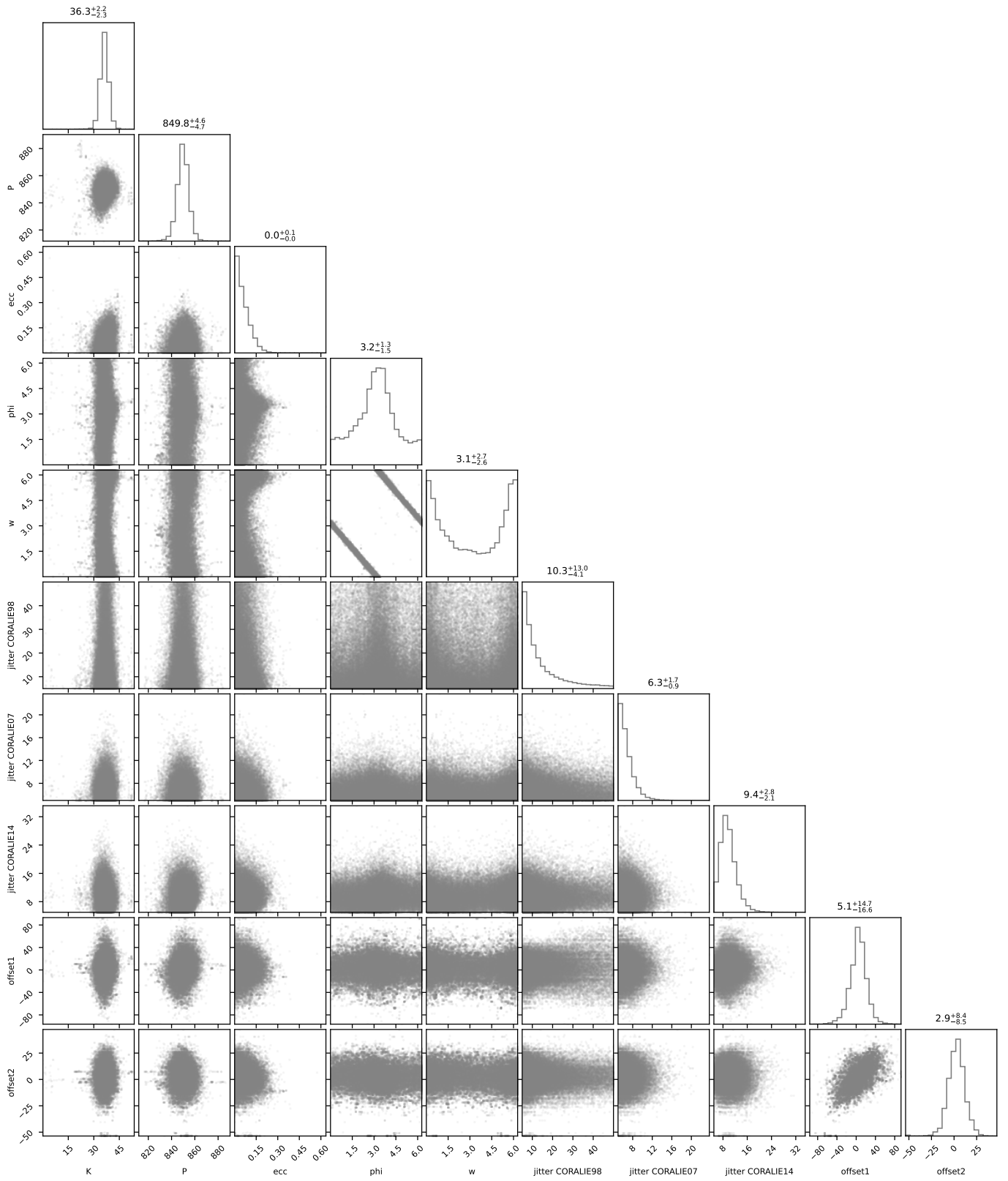


Fig. C.1: Corner plot of the parameters posterior distributions for the RV modelling with *kima* for HD 125136.

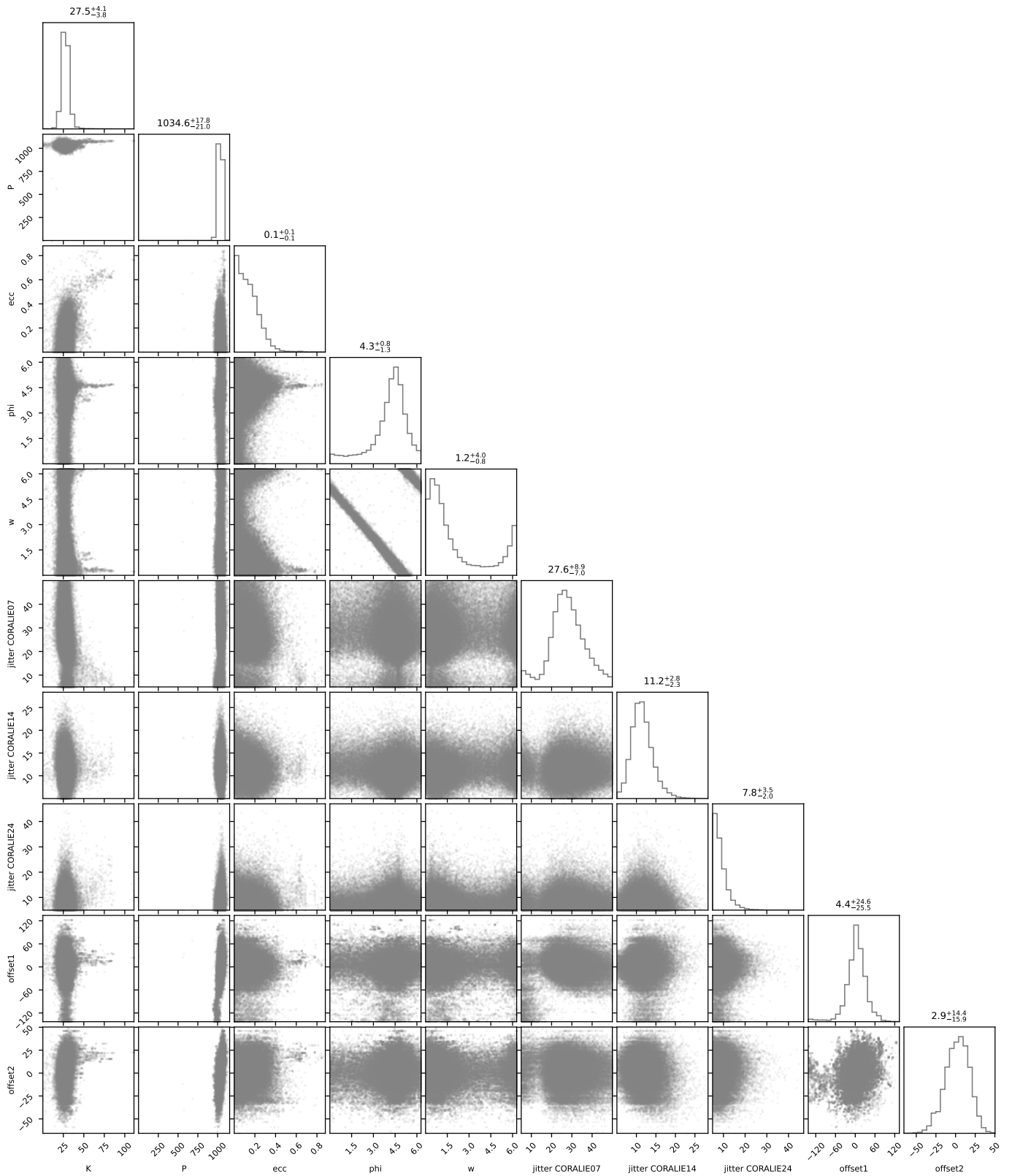


Fig. C.3: Same as Fig C.1 but for HD 220218.